ELSEVIER

Contents lists available at ScienceDirect

# Journal of Membrane Science

journal homepage: www.elsevier.com/locate/memsci





# Unlocking bulk and surface oxygen transport properties of mixed oxide-ion and electron conducting membranes with combined oxygen permeation cell and oxygen probe method

Yongliang Zhang, Kevin Huang

Department of Mechanical Engineering, University of South Carolina, Columbia, SC, 29201, USA

ARTICLE INFO

Keywords:
Oxygen permeation
Perovskite
Oxygen surface exchange
Oxygen diffusion

#### ABSTRACT

Surface exchange kinetics and bulk diffusion of oxygen are of paramount importance to the activity of oxygen electrocatalysis and performance of electrochemical devices such as fuel cell, metal-air batteries, and oxygen separation membranes. Conventional approaches to obtaining these transport properties are often limited to single property under a specific non-operation related condition. Here we use a combined oxygen permeation cell and oxygen probe methodology to simultaneously attain rates of oxygen surface exchange and bulk conductivity/chemical diffusivity of three representative mixed oxide-ion and electron conductors, namely  $SrCo_{0.9}Ta_{0.1}O_{3-\delta}$  (SCT),  $La_{0.6}Sr_{0.4}CoO_{3-\delta}$  (LSC) and  $La_{0.6}Sr_{0.4}FeO_{3-\delta}$  (LSF), operated under a steady-state oxygen flux. The results explicitly show that SCT exhibit the highest oxide-ion conductivity/chemical diffusivity, fastest rates of surface oxygen exchange kinetics, thus promising to be the best oxygen electrocatalyst. We have also mapped out the distribution of oxygen chemical potential gradient across the membranes and applied B-transport number concept to illustrate the rate-limiting steps in the overall oxygen permeation process.

# 1. Introduction

Oxygen-deficient perovskite or -related oxides are a family of excellent catalysts for oxygen electrocatalysis in electrochemical devices involving oxygen as an active species, such as reversible solid oxide cells (RSOCs) [1], rechargeable metal-air batteries (RMABs) [2], and oxygen transport membranes (OTMs) [3]. The high electrocatalytic activity in these materials is mostly understood to arise from their mixed electronic and oxide-ion conductivity. In general, these materials are electron-dominating conductors, but the magnitude of partial oxide-ion conductivity is much higher than that of pure oxide-ion conductors because of the enhanced oxide-ion transport by the overwhelming electron transport via the "drag-pull" mechanism to satisfy the local quasi charge-neutrality requirement [4]. While not fully understood, it is generally accepted that the higher the partial oxide-ion conductivity (or oxygen vacancy concentration) the better the oxygen electrocatalytic activity when used as an oxygen electrode. For example, a combination of larger A-site cations (e.g. Ba, Sr) with Co or Fe on the B-site in ABO<sub>3</sub> perovskites yields the highest partial oxide-ion conductivity along with the dominating electronic conductivity and the best oxygen electrocatalytic activity [5]. Theoretical and experimental studies both

suggested that the high oxygen vacancy concentration (thus partial oxide-ion conductivity) is fundamentally rooted in the strong orbital interactions between 3d electrons of Co(Fe) and 2p electrons of oxygen, which results in O-Co(Fe)-O bonds with heavy covalent character [6–8]. With a larger A-cation, the Goldschmidt tolerance factor is close to unit and the perovskite structure tends to be more cubic with a greater unit cell. In such a large cell, the O-Co(Fe)-O bond is stretched out and weakened, resulting in high propensity to lose oxygen at elevated temperatures. If the cubic structure could be maintained after oxygen loss at elevated temperatures (either during synthesis or operation), the significant amount of oxygen vacancies, thus high partial oxide-ion conductivity, would provide excellent oxygen electrocatalytic activity. Unfortunately, most of those perovskites with large A-cations and Co/Fe as B-cation cannot retain their cubic structure after losing significant amount of oxygen, transforming into other phases such as brownmillerite with ordered immobile oxygen vacancies, thus less oxygen electrocatalytic activity. In addition, the high concentration of oxygen vacancies in those materials can attract CO2 and H2O from ambient air, forming carbonates and hydroxides on their surfaces.

To best utilize these highly active oxygen-deficient  $ABO_{3-\delta}$  for practical applications, aliovalent doping at both A- and B-site is

E-mail address: huang46@cec.sc.edu (K. Huang).

<sup>\*</sup> Corresponding author.

commonly practiced. Representative of these stabilized oxygen-deficient ABO $_{3-\delta}$ , which have been widely used as practical catalysts for oxygen electrocatalysis in RSOCs, RMABs and OTMs, include, but not limited to, La $_{0.6}$ Sr $_{0.4}$ CoO $_{3-\delta}$  (LSC) [9,10], La $_{0.6}$ Sr $_{0.4}$ FeO $_{3-\delta}$  (LSF) [11] and SrCo $_{0.9}$ Ta $_{0.1}$ O $_{3-\delta}$  (SCT) [12–14]. While the electrochemical performance (e.g. polarization resistances and overpotentials) of these materials have been well documented in literature, their bulk and surface transport properties suited for explaining their true electrochemical behaviors in practical devices are still lacking.

In theory, there are two basic processes involved in oxygen electrocatalysis: surface oxygen exchanges and bulk oxygen diffusion. In the past, the rates of these two processes are often obtained by electrical conductivity relaxation (ECR) [15,16] and isotopic exchange depth profile (IEDP) method coupled with time-of-flight secondary ion mass spectroscopy (ToF-SIMS) [17]. One issue with such-obtained data is that they are only associated with one half of the oxygen electrocatalysis cycle, viz. either oxygen reduction reaction (ORR) or oxygen evolution reaction (OER) under equilibrium conditions, whereas most high-temperature electrochemical devices such as RSOCs, RMABs and OTMs operate under a steady-state oxygen flux (or current) but non-equilibrium state. Many years ago, Maier pointed out that oxygen permeation cell is the most reliable method to obtain more meaningful bulk properties such as partial oxide-ion conductivity and oxygen chemical diffusivity of electron-dominating mixed oxide-ion and electron conductors (MOECs) [18]. When using this method to extract surface exchange rate, however, the kinetics of ORR and OER must be assumed the same due to the lack of experimental methods to separate them. As an example, we have previously used a combined oxygen permeation cell and theoretical modeling to simulate oxygen transport through the bulk and surface of an OTM but had to assume that the surface exchange kinetic rates are the same for both ORR and OER [13]. Obviously, this is a rather weak assumption because the surface oxygen exchange kinetics varies with partial pressure of oxygen and the two opposing surfaces of an OTM are exposed to two very different oxygen partial pressures.

Here we report a full set of bulk and surface oxygen transport properties of LSC, LSF and SCT MOECs, including oxygen chemical potential gradient, oxygen permeation flux, partial oxide-ion conductivity, oxygen chemical diffusivity, and rates of oxygen surface exchange kinetics, obtained by a combined oxygen permeation cell (OPC) and oxygen probe (OP) approach. The obtained transport properties are then correlated with the known catalytic activity of the materials to further demonstrate the key factor determining the activity. Through three wellknown OTMs with very different oxygen transport properties, we also support the applicability of the OPC/OP method to other OTMs. The OPC/OP method used was originally proposed by Geffroy et al. [19-21], in which two sets of oxygen sensors were employed to the two opposing surfaces of an OTM to probe the surface chemical potential of oxygen, while oxygen permeation flux is being measured by an online gas chromatograph. From all the data collected, i.e. oxygen chemical potential gradients across the bulk and two surface layers and steady-state oxygen permeation flux, bulk partial oxide-ion conductivity/oxygen chemical diffusivity and rate of individual surface oxygen exchange kinetics as a function of temperature and partial pressure of oxygen are obtained. Based on the above results, the rate limiting steps in the overall oxygen permeation process are discussed.

#### 2. Theoretical background of the methodology

The gradient of chemical potential of oxygen  $(\Delta\mu_{O_2})$  across an OTM is the driving force for the oxygen permeation. The core of the Geffroy's method is to use oxygen sensor to probe  $\mu_{O_2}$  (or  $\Delta\mu_{O_2}$  in relative to the oxygen chemical potential of feed-gas (air),  $\mu_{O_2}^{g-ORR}$ ) at the two surfaces. Fig. 1 schematically illustrates a distribution profile of oxygen chemical potential gradient across the OTM. The governing equations for  $\Delta\mu_{O_2}$  in

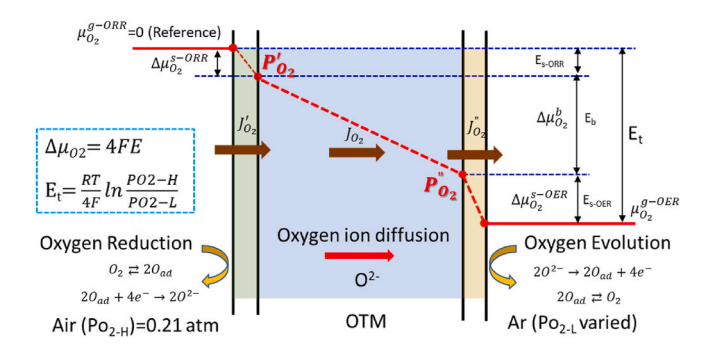


Fig. 1. Illustration of distribution profiles of oxygen chemical potential gradients across an OTM.

each layer are given by Nernst equation:

$$\Delta \mu_{O_2}^{s-ORR} = 4FE_{s-ORR} \tag{1}$$

$$\Delta \mu_{O_2}^{s-OER} = 4FE_{s-OER} \tag{2}$$

$$\Delta \mu_{O_{\tau}}^{b} = 4FE_{b} = 4F(E_{t} - E_{s-ORR} - E_{s-OER})$$
(3)

where  $\Delta\mu_{O_2}^{s-ORR}$  and  $\Delta\mu_{O_2}^{s-OER}$  are the gradients of oxygen chemical potential across ORR and OER surface layers, respectively;  $E_{s-ORR}$  and  $E_{s-OER}$  are the corresponding Nernst potential (or electromotive force, EMF), respectively;  $\Delta\mu_{O_2}^b$  and  $E_b$  are the gradient of oxygen chemical potential across the membrane bulk and the corresponding Nernst potential, respectively;  $E_t$  is calculated by:

$$E_{t} = \frac{RT}{4F} ln \frac{P_{O2-H}}{P_{O2-L}} \tag{4}$$

where  $P_{O_2-H}$  is the partial pressure of oxygen fixed at 0.21 atm at the ORR side and  $P_{O_2-L}$  is the partial pressure of oxygen at the OER side, which is measured by gas chromatograph.

For conditions close to the equilibrium under which the rates of forward and backward surface oxygen reactions are equal, one can represent oxygen flux through the two surfaces by Onsager equation [22]:

$$J'_{O_2} = j'_{ex} \frac{\Delta \mu_{O_2}^{s-ORR}}{RT} \tag{5}$$

$$J_{O_2}'' = j_{ex}'' \frac{\Delta \mu_{O_2}^{s-OER}}{RT} \tag{6}$$

Here  $j_{ex}'$  and  $j_{ex}''$  (mol  $O_2$  cm<sup>-2</sup> s<sup>-1</sup>) are the balanced oxygen exchange rates at the ORR and OER surfaces, respectively, under no oxygen potential gradients. R and T are gas constant and temperature in K, respectively.

Under non-equilibrium conditions, *i.e.* when a net oxygen flux passes through the membrane, eqs. (5) and (6) needs to be modified to reflect the net oxygen flux resulted from nonequal rates of forward and backward surface oxygen reactions. For ORR reaction,  $O + 2e \Rightarrow O^{2-}$ , the net oxygen flux  $J_O$  across the surface equals forward oxygen flux  $J_O^f$  subtracted by backward oxygen flux  $J_O^b$ ,  $J_O = J_O^f - J_O^b$ . From the generic definitions of  $J_O$  and k [23], we have

$$J_O = KC(0,t) = C(0,t)k^0 \exp\left[-\frac{\Delta G^{\neq}}{RT}\right]$$
 (7)

where C(0, t) is the surface concentration of active species;  $k^0$  is the standard rate constant of oxygen exchange reaction at equilibrium;  $\Delta G^{\neq}$  is the standard Gibbs free energy for activating the active species. Factoring in transfer coefficient  $\alpha$  to account for asymmetry caused by

the shift of activation Gibbs free energy under a net oxygen flux, we have for oxygen flux  $J_O$  through the ORR surface

$$J_{O}^{'}=2J_{O_{2}}^{'}=k_{f}C_{O}(0,t)-k_{b}C_{R}(0,t)$$

$$K_{ORR} \left[ C_O(0, t) \exp\left(-\frac{\alpha \Delta \mu_O^{s-ORR}}{RT}\right) - C_R(0, t) \exp\left(\frac{\left(1 - \alpha\right) \Delta \mu_O^{s-ORR}}{RT}\right) \right]$$
(8)

$$K_{ORR} \left[ C_O(0, t) \exp\left(-\frac{\alpha \Delta \mu_{O_2}^{s-ORR}}{2RT}\right) - C_R(0, t) \exp\left(\frac{\left(1 - \alpha\right) \Delta \mu_{O_2}^{s-ORR}}{2RT}\right) \right]$$

Here  $\Delta\mu_O^{s-ORR}=\frac{1}{2}\Delta\mu_{O_2}^{s-ORR}$ ;  $K_{ORR}$  is the rate constant of oxygen surface exchange at the feed-side. The transfer coefficient  $\alpha$  is an indicator of the symmetry of the energy barrier for activation polarization. For MOECs, it has been suggested that  $\alpha=0.5$  [20,23], which means a symmetrical  $\Delta G^{\neq}$  profile vs. reaction coordinate or a symmetrical energy barrier for activation polarization.  $C_O(0,t)$  equals  $C_O^b(T,P_{O_2})$  at  $P_{O_2}=0.21$  atm;  $C_R(0,t)$  equals  $C_O^b(T,P_{O_2})$  at  $P_{O_3}$ ;  $C_O^b(T,P_{O_2})$  can be calculated by

$$C_O^b(T, P_{O_2}) = \frac{3 - \delta(T, P_{O_2})}{V_m N_A}$$
 (9)

where  $N_A$  is Avogadro constant (6.02 ×  $10^{23}$ /mol);  $V_m$  (cm³) and  $\delta$  are the unit cell volume and oxygen non-stoichiometry of the membrane, respectively. The  $\delta$  (T,  $P_{O_2}$ ) for SCT is available from our previous work [24], and  $\delta$  (T,  $P_{O_2}$ ) for LSF and LSC are taken from Ref. [25] and Ref [26], respectively.

Similarly, for OER,  $O^{2-} = O + 2e$ , the oxygen flux  $J_O^*$  across the OER surface is given by:

$$\begin{split} J_O^- &= 2J_{O_2}^- = k_f C_R(0,t) - k_b C_O(0,t) \\ K_{OER} \left[ C_R(0,t) \exp\left(\frac{\left(1-\alpha\right)\Delta\mu_O^{s-OER}}{RT}\right) - C_O(0,t) \exp\left(-\frac{\alpha\Delta\mu_O^{s-OER}}{RT}\right) \right] \\ K_{OER} \left[ C_R(0,t) \exp\left(\frac{\left(1-\alpha\right)\Delta\mu_O^{s-OER}}{2RT}\right) - C_O(0,t) \exp\left(-\frac{\alpha\Delta\mu_O^{s-OER}}{2RT}\right) \right] \end{split}$$

Here  $\Delta\mu_O^{s-OER}=\frac{1}{2}\Delta\mu_O^{s-OER}$ ;  $C_R(0,t)$  equals  $C_O^b(T,P_{O_2})$  at  $P_{O_2}''$ ;  $C_O(0,t)$  equals  $C_O^b(T,P_{O_2})$  at  $P_{O_2}=P_{O_2-L}$ ;  $K_{OER}$  is the rate constant of oxygen surface exchange at the sweep-side. For MOEC membranes [17,27,28],  $K_{OER}$  and  $K_{ORR}$  are the function of  $P_{O_2}$  and T, and follow a power law of  $K=K_0(P_{O_2}/P_{O_2}^0)^{\rm m}$ . Here  $K_0$  is the rate constant under the reference oxygen partial pressure,  $P_{O_2}^0=0.21$  atm; m is the power index.

At steady state of oxygen permeation,

$$J'_{O_2} = J''_{O_2} = J_{O_2} \tag{11}$$

$$J_{O_2} = \frac{\sigma_i(T, P_{O_2})}{16F^2L} \Delta \mu_{O_2}^b = \frac{\widetilde{D}_O(T, P_{O_2})C_O^b(T, P_{O_2})}{4LRT} \Delta \mu_{O_2}^b$$
 (12)

where  $J_{O_2}$  is the oxygen flux passing the bulk of the membrane;  $\sigma_i = \sigma_i(T, P_{O_2})$  is the partial oxide-ion conductivity in OTM;  $\widetilde{D}_{\rm O} = \widetilde{D}_{\rm O}(T, P_{O_2}) = \frac{RT\sigma_i(T,P_{O_2})}{4F^2C_0^b(T,P_{O_2})}$  (cm²/s) is the corresponding chemical diffusivity of oxygen.

With the measured  $J_{O_2}$ ,  $\Delta \mu_{O_2}^{s-ORR}$ , and  $\Delta \mu_{O_2}^{s-OER}$ , we can calculate  $K_{ORR}$ ,  $K_{OER}$  and  $\sigma_i$  ( $\widetilde{D}_O$ ), according to eqs. (8), (10) and (12), respectively.

It is to be noted that the linear surface flux equations (5) and (6) under equilibrium condition are only valid when  $P_{O_2}$  range within the two surface layers is small enough to satisfy the condition of  $\Delta\mu_{O_2}^{s-ORR}$  and  $\Delta\mu_{O_2}^{s-ORR}$  «RT [22]. However, we will show that this condition cannot be met in this study due to the large oxygen partial pressure gradient observed. To fairly assess the rate-limiting steps in the overall oxygen permeation process, we adopt the B transport number concept proposed by Geoffroy et al. [21] and further used by Kagomiya et al. [29] The

definitions of B-transport numbers are:

$$B_C = \frac{\Delta \mu_{O2}^{s-ORR} + \Delta \mu_{O2}^{s-ORR}}{\Delta \mu_{O2}^b} \tag{13}$$

$$B_{C-ORR} = \frac{\Delta \mu_{O2}^{s-ORR}}{\Delta \mu_{O2}^b} \tag{14}$$

$$B_{C-OER} = \frac{\Delta \mu_{OO}^{S-OER}}{\Delta \mu_{OO}^b} \tag{15}$$

where  $B_C$  is the total surface transport number;  $B_{C-ORR}$  and  $B_{C-OER}$  are the individual surface transport numbers for ORR and OER surfaces, respectively. The magnitude of  $B_C$  can provide some hints for rate limiting steps. For example, 1) when  $B_C\gg 1$ , the rate limiting step is oxygen surface exchange; 2) when  $B_C\ll 1$ , the rate limiting step is oxygen bulk diffusion; and 3) when  $B_C\approx 1$ , both oxygen surface exchange and oxygen bulk diffusion would involve in the limitation of oxygen flux. In addition, with  $B_{C-ORR}$  and  $B_{C-OER}$ , one can further specify whether ORR or OER predominates the total surface oxygen exchange processes.

# 3. Experimental procedures

### 3.1. Membrane synthesis

SCT, LSC and LSF were prepared by solid-state reaction method. First, stoichiometric amounts of La<sub>2</sub>O<sub>3</sub> (99.99%, Sigma Aldrich, after drying at 1000 °C for 5 h), SrCO<sub>3</sub> (≥99.9%, Sigma Aldrich), Co<sub>3</sub>O<sub>4</sub> (99.7%, Alfa Aesar), Fe<sub>2</sub>O<sub>3</sub> (99.7%, Alfa Aesar), Ta<sub>2</sub>O<sub>5</sub> (99.85%, Alfa Aesar) for SCT, LSC and LSF were first ball-milled in ethanol for 3 h, followed by drying and calcining at 1000 °C with heating and cooling rates of 3 °C min<sup>-1</sup>, respectively, for 10 h. Next, the as-calcined powders were ball-milled, dried, and calcined at 1050  $^{\circ}\text{C}$  for another 10 h to further enhance the phase purity and homogeneity. Finally, the powders were ball-milled, dried, and pressed into a pellet with a diameter of 2.54 cm and thickness of 1.5 mm and sintered at 1200 °C (for LSF and LSC) or 1220 °C (for SCT) for 10 h, respectively, at heating and cooling rates of 2 °C min<sup>-1</sup>. The obtained membranes all have a density greater than 98%. The two surfaces of dense pellets were then polished with SiC sandpaper from 200 to 1000 mesh to remove any surface contaminations.

### 3.2. Phase purity analysis

The phase purity of samples was examined by an X-ray diffractom-eter (XRD, Rigaku) equipped with graphite-monochromatized Cu K $\alpha$  radiation ( $\lambda=1.5418$  Å) over a  $2\theta$  range of  $10\text{--}80^{\circ}$  in a step size of  $5^{\circ}\text{-min}^{-1}$ .

# 3.3. Electrical conductivity measurement

Bar samples with a dimension of 45 mm  $\times$  6 mm  $\times$  4 mm sintered at the same temperatures above were attached with two voltage tabs and two current tabs for total electrical conductivity measurement. The total conductivity was measured vs. T in air using CorrWare software within a Solartron 1287/1260 electrochemical system. During measurement, a constant current (I) was applied across the sample while the voltage drop across the two voltage tabs was measured. The temperature of interest for this study ranged from 500 to 800 °C in a 50 °C interval.

# 3.4. Oxygen permeation flux and chemical potentials measurement

A commercial Probostat (NorECs Ltd.) was used to measure oxygen permeation flux and surface chemical potentials of the membranes. Fig. 2 shows a schematic of the system. The dense membrane with a silver ring as the sealant was first placed on the top of a thick-wall  ${\rm Al}_2{\rm O}_3$ 

(10)

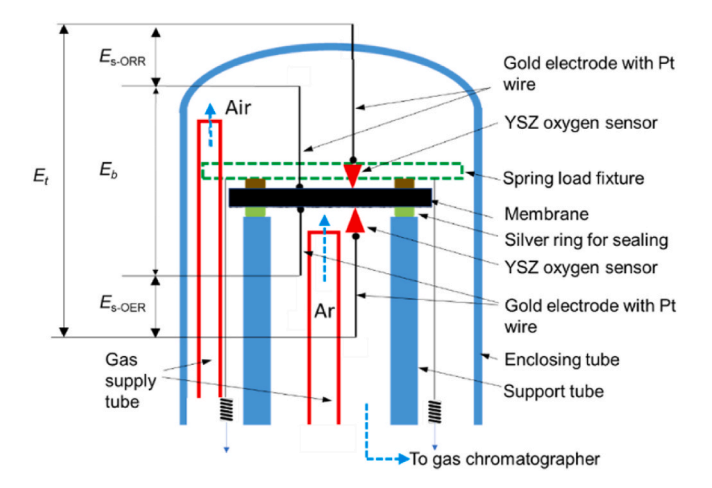


**Fig. 2.** Schematic of experimental setup for simultaneously measuring oxygen permeation flux and oxygen chemical potentials at different locations.

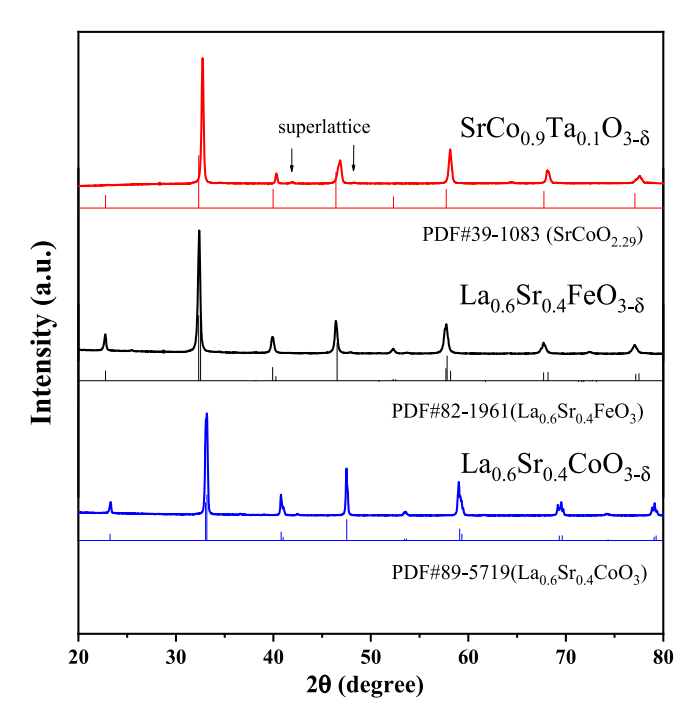
support tube, followed by applying spring load. To ensure a good sealing, we have also applied additional layer of silver paste (DAD-87, Shanghai Research Institute of Synthetic Resins) on the edge of the membrane/silver ring/tube interface. To measure  $\Delta\mu_{O_2}^{s-ORR}$  and  $\Delta\mu_{O_2}^{s-OER}$ , two microscale yttrium-stabilized zirconia (YSZ) oxygen probes with a gold electrode pasted on the flat side were gently pressed against the two opposing surfaces of the membrane, while two other gold electrodes were pasted as a point directly on the membrane surfaces for bulk voltage measurement. Three voltages, shown in Fig. 2, viz.  $E_{s\text{-}ORR}$ ,  $E_{s\text{-}OER}$  and  $E_b$ , were measured by a high-resolution digital multimeter (Agilent, model 34401A,  $6\frac{1}{2}$  digital). The  $E_{s\text{-}ORR}$  on the feed surface and  $E_{s\text{-}OER}$  on the sweep surface are a direct measurement of kinetic resistance attributed to oxygen surface exchanges.

During a typical run, the system was first gradually heated up to 920 °C at a rate of 1 °C min  $^{-1}$  and held for 1 h to ensure a tight gas seal. The feed side of the membrane is flowed with air in an enclosing alumina tube, while the sweep side is flowed with an ultra-pure Ar inside the support tube. For oxygen permeation flux measurement, the flow rate of feed gas air is fixed at 100 sccm, and that of sweep Ar gas is varied from 10 to 150 sccm to achieve different  $P_{O_2}$ . The sweep gas with the permeated oxygen was then analyzed by an on-line gas chromatograph (490 Micro GC, Agilent Inc.) to obtain  $P_{O_2-L}$ ,  $E_t$  and  $J_{O_2}$ . Control of airleakage is critically important for this experiment to ensure the accuracy and reliability of the data. Therefore, for any experiments showing air leakage greater than 1%, the data will be discarded. For those accepted data, the leakage corrections were performed on both oxygen flux and EMF calculations. For each OTM composition, we prepared 2-3 samples and performed the experiment with each sample to ensure the repeatability and accuracy of the data.

### 4. Result and discussion

#### 4.1. Phase purity

The desirable single-phase perovskite structure of SCT, LSF and LSC are confirmed in Fig. 3 of XRD patterns collected at room temperature by their excellent match with the PDF card of each sample. Specifically, SCT has a primitive cubic structure (S.G.: Pm-3m), while LSF and LSC have orthorhombic structure (S.G.: R–3C). The left-shift of 20 in SCT pattern compared to pure  $SrCoO_{2.29}$  is caused by the larger  $Ta^{5+}$  doping ( $Ta^{5+}$ : 0.78 Å vs.  $Co^{4+}$ : 0.67 Å for CN=6). There are also two weak peaks at  $42^{\rm o}$  and  $48.5^{\rm o}$  identified on SCT pattern, which is an indicative of oxygen-ordered superlattice in tetragonal (S.G.: P4/mmm) structure. We confirmed from a previous study on a similar  $SrCo_{0.9}Nb_{0.1}O_{3-\delta}$  system that this superlattice phase will disappear at higher temperatures as the



 $\begin{tabular}{lll} Fig. & 3. & XRD & patterns & of sintered & SCT, & LSC & and & LSF & collected & at room temperature. \\ \end{tabular}$ 

ordered oxygen dissociates [30].

### 4.2. Oxygen bulk transport properties

The raw data collected in this experiment include oxygen concentration in Ar-sweep gas at different flow rates,  $E_{s\text{-}ORR}$  and  $E_{s\text{-}OER}$ . According to the continuous stirred-tank reactor (CSTR) model, varying sweep gas flow rates will result in change in oxygen contents in Arsweep gas, thus change in oxygen chemical potential gradients ( $\Delta\mu_{O_2}$ ) and oxygen permeation flux ( $J_{O_2}$ ) across the membrane. Since  $P_{O_2-L}$  varies with the type of membranes at a given Ar-flow, we use the Ar-flow to represent  $P_{O_2-L}$  for the transport data presentations throughout the paper.

Fig. 4(a-1), (b-1) and (c-1) show the measured  $E_{s\text{-}ORR}$  and  $E_{s\text{-}OER}$ , and the calculated  $E_b$  using eqs. (3) and (4) of the three OTMs at different conditions. In most cases, as Ar flow increases and temperature decreases,  $E_{s\text{-}OER}$  and  $E_b$  rise. This is because a higher Ar flow (or lower  $P_{O_2-L}$ ) will create a greater  $\Delta\mu$  across the membrane, which will directly affect  $E_{s\text{-}OER}$  at the sweep side and then  $E_b$  across the membrane bulk. The Ar-flow has a relatively little effect on  $E_{s\text{-}ORR}$  because  $E_{s\text{-}OER}$  and  $E_b$  are the rate-limiting step (RLS), and the feed gas can provide sufficient oxygen at the ORR surface. The trends of  $E_{s\text{-}OER}$  and  $E_b$  at different  $E_s$  are also reasonable since a higher  $E_s$  will accelerate the oxygen desorption and ion transport.

However, there are a few of opposite trends observed, one is the increase of  $E_{s\text{-}ORR}$  with T for SCT. Generally, a high T will favor the reactions, thus lowering  $E_{s\text{-}ORR}$ . The opposite trend here can be ascribed to the excellent ORR activity of the SCT. It can be seen from later Fig. 8 that  $E_a$  for SCT's ORR is very small, suggesting that ORR is insensitive to T. At low T, the bulk oxygen transport is slower, resulting in an accumulation of  $O_2$  at the surface, and thus making  $E_{s\text{-}ORR}$  small. As T increases, the bulk oxygen transport is accelerated, resulting in lower surface  $O_2$  and a greater  $E_{s\text{-}ORR}$ .  $E_{s\text{-}ORR}$  for LSC also has a slight increase with T, though the trend is not as obvious as SCT. For LSF, the  $E_{s\text{-}ORR}$  has a normal trend and decreases with T just as  $E_{s\text{-}OER}$ . But  $E_b$  for LSF tends to increase with T at higher Ar flow. Note that at higher Ar-flow and lower T, OER becomes a RLS for LSF, to be discussed in the following section (section 4.5). The opposite trend of  $E_b$  can be related to the drastic decrease of  $E_{s\text{-}OER}$  with

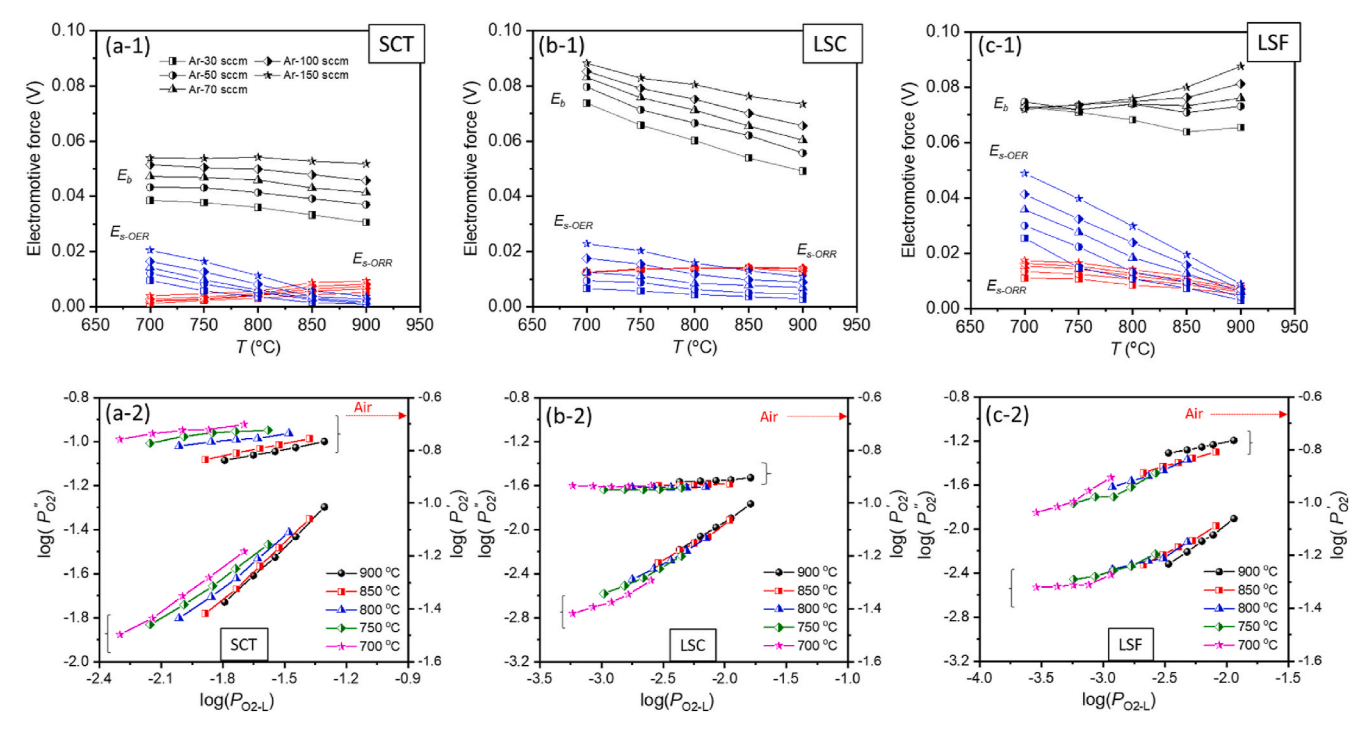


Fig. 4. Electromotive forces ( $E_b$  -black,  $E_{s-ORR}$  -red and  $E_{s-ORR}$  -blue) vs. T of (a-1) SCT; (b-1) LSC and (c-1) LSF at different Ar flows. Interfacial  $P_{O_2}$  vs. sweep-side  $P_{O_2-L}$  at different T. (a-2) SCT; (b-2) LSC; (c-2) LSF. (For interpretation of the references to colour in this figure legend, the reader is referred to the Web version of this article.)

T, which will accelerate the  $O_2$  desorption at OER surface and increase  $P_{O_2}$  gradient in the bulk, resulting in a greater  $E_b$ . Overall, it seems that RLS plays a key role in the trending of EMF with T and Ar-flow ( $P_{O_2-L}$ ). Fig. 4(a-2), (b-2) and (c-2) show the variations of interfacial  $P_{O_2}$  across the membrane using the measured  $E_{s\text{-ORR}}$  and  $E_{s\text{-OER}}$  in the Nernst equation in response to the change of Ar-flow ( $P_{O_2-L}$ ) at the Ar sweep

side. The notations of interfacial  $P_{O_2}$  are given in Fig. 1. For the OER surface, increasing T raises  $P_{O_2}^{"}$  at a given Ar-flow for all three OTMs, while shifting  $P_{O_2-L}$  range toward higher end. The T-enhanced oxygen flux is clearly the reason for this trending; this indicates that increasing T will favor promoting the RLS. The following sections (section 4.5) will give a more detailed discussion on the temperature related RLS.

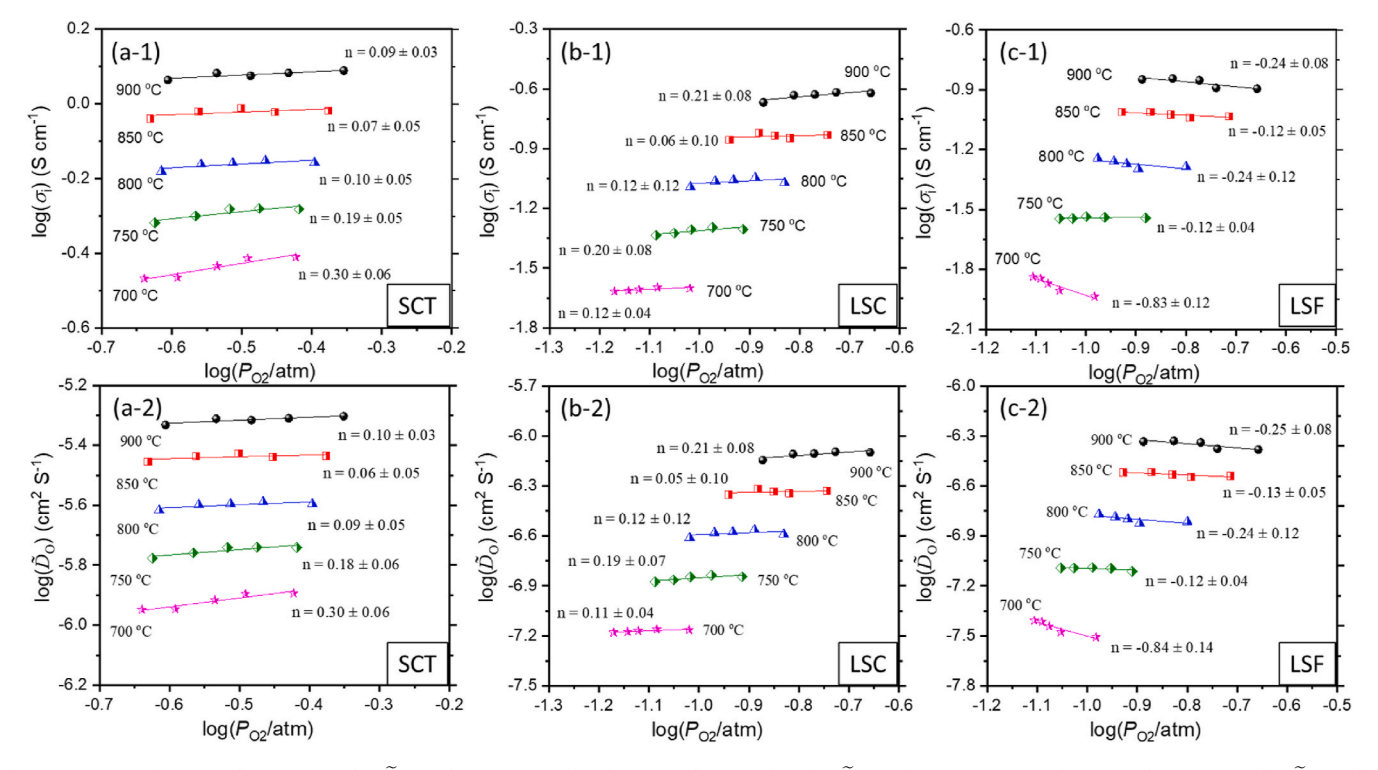


Fig. 5. SCT: (a-1)  $\log(\sigma_i)$  vs.  $\log P_{O_2}$ ; (a-2)  $\log(\widetilde{D}_O)$  vs.  $\log P_{O_2}$ . LSC: (b-1)  $\log(\sigma_i)$  vs.  $\log P_{O_2}$ ; (b-2)  $\log(\widetilde{D}_O)$  vs.  $\log P_{O_2}$ . LSF: (c-1)  $\log(\sigma_i)$  vs.  $\log P_{O_2}$ ; (c-2)  $\log(\widetilde{D}_O)$  vs.  $\log P_{O_2}$ . All at different temperatures and  $\widetilde{D}_O(T, P_{O_2}) = \frac{RT\sigma_i(T, P_{O_2})}{4F^2C_O^k(T, P_{O_2})}$ .

However, for  $P_{O_2}'$  at the ORR surface, the three OTMs show different trending: 1) SCT's  $P_{O_2}'$  slightly decreases with decreasing  $P_{O_2-L}$  and increasing temperature; 2) LSC's  $P_{O_2}'$  is nearly independent of  $P_{O_2-L}$  and temperature; 3) LSF's  $P_{O_2}'$  decreases with  $P_{O_2-L}$  but increases with temperature. Since these  $P_{O_2}'$  are directly derived from  $E_{s\text{-ORR}}$  (or  $\Delta\mu_{O_2}^{s\text{-ORR}}$ ) data, these trends are also reflected in  $\Delta\mu_{O_2}^{s\text{-ORR}}$  to be shown later in Fig. 9. The different trending in different OTMs is believed to stem from the intrinsic charge transport properties of each material, which ultimately determine the magnitudes of bulk oxygen diffusion and surface oxygen exchange kinetics. We will discuss these in the following sections.

The log-log plots between  $\sigma_i$  and  $P_{O_2}$  are shown in the first row of Fig. 5, assuming power law relationship of  $\sigma_i = \sigma_i^o P_{O_2}^n$ , where  $\sigma_i^o$  and n are constants. To obtain  $\sigma_{\rm i}$ , we use eq. (12) since both  $J_{O_2}$  and  $\Delta\mu_{O_2}^b$  are measured as a function of temperature and  $P_{O_2-L}$ . Since the membrane is subject to a gradient between  $P_{O_2}^{'}$  and  $P_{O_2}^{''}$ , we take the geometric mean  $(P'_{O_2}P''_{O_2})^{1/2}$  as the averaged  $P_{O_2}$  plotted against  $\sigma_i$  in Fig. 5; this treatment assumes a linear  $\Delta\mu$   $\sim$  ln $P_{O_2}$  profile across the membrane. From the obtained  $\sigma_i$ , we further calculate out oxygen chemical diffusivity of  $\widetilde{D}_0$ from Nernst-Einstein equation embedded in eq. (12), which are shown in the second row of Fig. 5. In general,  $\sigma_i$  and  $\widetilde{D}_0$  have expectedly a similar trend and power index (n) for each material. For different materials, however, the order of magnitude and power index vary significantly. For example, SCT and LSC show small and positive n-value, which are not varying significantly within the standard deviation limit. The n > 0 implies that a higher  $P_{O_2}$  favors a higher  $\sigma_i$ . This is expected for p-type conductors like SCT and LSC since their higher electronic conductivity at higher  $P_{O_2}$  promotes oxide-ion conductivity through the "drag-pull" effect. For LSF, however, n < 0 is observed. This opposite trending to SCT and LSC is resulted from LSF's electronic conduction changing from p-type to n-type at lower  $P_{O_2}$  range [10]. We acknowledge that LSF's 700 °C-data are not very reliable due to its very low oxygen flux. Overall, SCT has the highest  $\sigma_i$  and  $\widetilde{D}_{O_i}$ , followed by LSC and LSF. This observation agrees with the trend observed for oxygen vacancy concentration [20,24,25].

The Arrhenius plots of  $\sigma_i$  of the three materials are shown in Fig. 6(a). Note that the data plotted are those from  $P_{O_2}$  at Ar flow of 100 sccm for illustration purpose. As shown in Fig. 5(a),  $\sigma_i$  generally has a weak dependence on  $P_{O_2}$ . Thus, one would expect a similar Arrhenius relationship for other  $P_{O_2}$ . It is evident that SCT exhibits the lowest activation energy of 0.69 eV vs. 1.21 eV for LSC and 1.25 eV for LSF, suggesting that SCT is the most oxide-ion transport friendly material, particularly at lower temperature range. The total electrical conductivity ( $\sigma$ ) as well as ion transport number of SCT, LSC and LSF measured in air as a function of temperature are compared in Fig. S1. All samples

exhibit  $\sigma > 100$  S cm<sup>-1</sup>, generally suitable for using as OTMs or oxygen electrodes of RSOFC or RMABs. In addition, LSC shows the highest  $\sigma$  and behaves like a metal. While SCT exhibits a moderate  $\sigma$ , its ionic conductivity  $\sigma_i$  are the highest among the three materials, ranging from 0.3~1.2 S/cm at 600–900 °C, roughly 6–8 times higher than LSC and LSF. The  $\sigma_i$  values of SCT are very close to what have been previously reported using the same oxygen permeation cell (OPC) method [13]. Similarly, the measured  $\sigma_i$  of LSC, 0.024 ~ 0.24 S/cm from 700 to 900 °C, are also close to 0.025 ~ 0.20 S/cm from 730 to 890 °C reported in Ref. [31] using the same OPC method. For LSF, the only  $\sigma_i$  reported using ECR method varied from 0.013 ~ 0.049 S/cm from 800 to 900 °C [32], comparable to 0.057–0.14 S/cm for the same T range. Nevertheless, electrons holes or excess electrons are clearly the dominating charge carriers for the total electrical conduction of these materials.

Fig. 6(b) shows the Arrhenius plot of  $\widetilde{D}_{O}$  of the three materials. The trend of activation energy  $E_{a}$  follows that of  $\sigma_{i}$ .  $\widetilde{D}_{O}$  is in the order of magnitude of  $\sim 10^{-6}$  cm<sup>2</sup>/s for SCT, which is close to the reported 0.65  $\times$  10<sup>-6</sup> cm<sup>2</sup>/s using the same OPC method [13], and  $\sim 10^{-7}$  cm<sup>2</sup>/s for LSC and LSF within 700–900 °C. The latter values are comparable to those reported in the literature. For example, a similar  $\widetilde{D}_{O}$  for LSC ranging from 0.46 to 3.70  $\times$  10<sup>-7</sup> cm<sup>2</sup>/s was reported for 700–900 °C using ECR method [33]. Using the same method as this study, Derozier et al. reported similar  $\widetilde{D}_{O}$  =(3(±2) $\sim$ 6(±2))  $\times$  10<sup>-7</sup> cm<sup>2</sup>/s for La<sub>0.5</sub>Sr<sub>0.5</sub>FeO<sub>3-δ</sub> and La<sub>0.7</sub>Sr<sub>0.3</sub>FeO<sub>3-δ</sub> at 900 °C [34]. For easy reference, we have also summarized in Table 1 the analytical expressions of  $\sigma_{i}T$ ,  $\widetilde{D}_{O}$ ,  $K_{ORR}$  and  $K_{OER}$  in the form of AP<sub>O2</sub> <sup>m(n)</sup> exp(- $E_{a}/RT$ ); Fig. S1 gives an example of the data processing procedure.

#### 4.3. Oxygen surface exchange properties

Since  $\Delta\mu_{O_2}^{s_-ORR}$  and  $\Delta\mu_{O_2}^{s_-OER}$  are greater than RT under most conditions of this study, see below, we cannot use linearized  $J_{O_2}$ - $\Delta\mu_{O_2}^{s}$  equations to obtain  $K_{ORR}$  and  $K_{OER}$ . Instead, we used the more general B–V like kinetic rate eqs. (8) and (10) to calculate rates of surface oxygen exchange from the measured  $\Delta\mu_{O_2}^{s_-ORR}$  and  $\Delta\mu_{O_2}^{s_-OER}$ , and the known T- and  $P_{O_2}$ -dependent  $C_O(0, t)$  and  $C_R(0, t)$ . We take the geometric mean of  $P_{O_2-H}$  and  $P'_{O_2}$  to represent  $P_{O_2}$  at the ORR surface, and  $P_{O_2-L}$  and  $P'_{O_2}$  to represent  $P_{O_2}$  at the OER surface in the plots. We also use eq. (9) to calculate  $C_O(0, t)$  and  $C_R(0, t)$  at the averaged  $P_{O_2}$ . The two sets of kinetic exchange rates,  $K_{ORR}$  and  $K_{OER}$  in logarithmic format, of the three materials are plotted in the first and second rows of Fig. 7, respectively, as a function of log  $P_{O_2}$  at different temperatures, in expectation of power law relationship. Indeed, a linear dependence is generally observed for each material at a given T.

The positive dependence of  $K_{ORR}$  and  $K_{OER}$  on T of all samples shown in the first row of Fig. 7 is well expected given the thermally activated

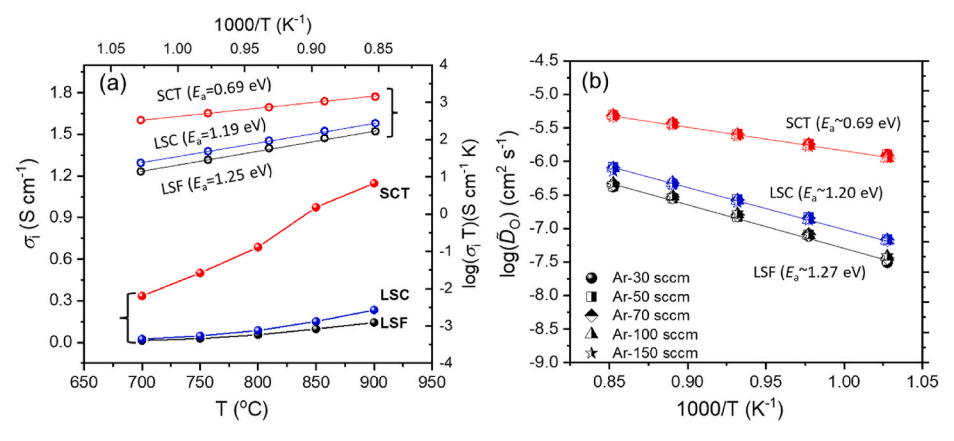


Fig. 6. (a) Regular and Arrhenius plot of  $\sigma_i$  at Ar flow of 100 sccm; (b) corresponding  $\widetilde{D}_0$  plots for SCT, LSC and LSF.

**Table 1** Analytical expressions of  $\sigma_i T$ ,  $\widetilde{D}_O$ ,  $K_{ORR}$  and  $K_{OER}$  of SCT, LSC and LSF in the form of  $AP_{O_2}^{n(m)}$ exp(- $E_a/RT$ ), where A,  $E_a$  and n/m are constants.

		σ <sub>i</sub> T (SK/cm)	$\widetilde{D}_{\mathrm{O}}$ (cm <sup>2</sup> /s)	$K_{OER}$ (cm/s)	$K_{ORR}$ (cm/s) <sup>a</sup>
E <sub>a</sub> (eV)	SCT	0.69(±0.03)	0.69(±0.03)	1.65(±0.09)	0.11(±0.10)
	LSC	$1.19(\pm 0.02)$	$1.20(\pm 0.02)$	$1.43(\pm 0.06)$	$1.02(\pm0.03)$
	LSF	$1.25(\pm 0.03)$	$1.27(\pm 0.03)$	$2.18(\pm0.04)$	$1.66(\pm 0.05)$
n/m	SCT	0.07 ~0.30	0.06 ~0.30	0.01 ~0.97	1.00 ~14.73
	LSC	$0.06 \sim 0.21$	$0.05 \sim 0.21$	0.51 ~1.10	$-56.09 \sim -8.30$
	LSF	$-1.06 \sim -0.12$	$-1.06\sim-0.12$	0.21 ~0.50	0.11 ~2.45
A	SCT	$1.64(\pm0.22)\times10^6$	$5.44(\pm0.86)\times10^{-3}$	$3.79(\pm 1.10) \times 10^4$	$8.96(\pm 3.34) \times 10^2$
	LSC	$5.49(\pm 1.11) \times 10^7$	$1.40(\pm0.25)\times10^{-1}$	$2.40(\pm 1.4) \times 10^3$	$2.39(\pm 2.38) \times 10^{-2}$
	LSF	$2.73(\pm0.44)\times10^{7}$	$5.96(\pm0.95) \times 10^{-2}$	$1.09(\pm 0.39) \times 10^6$	$6.15(\pm 1.79) \times 10^2$

<sup>&</sup>lt;sup>a</sup> These data might not be reliable due to the limitation of the method.

Y. Zhang and K. Huang

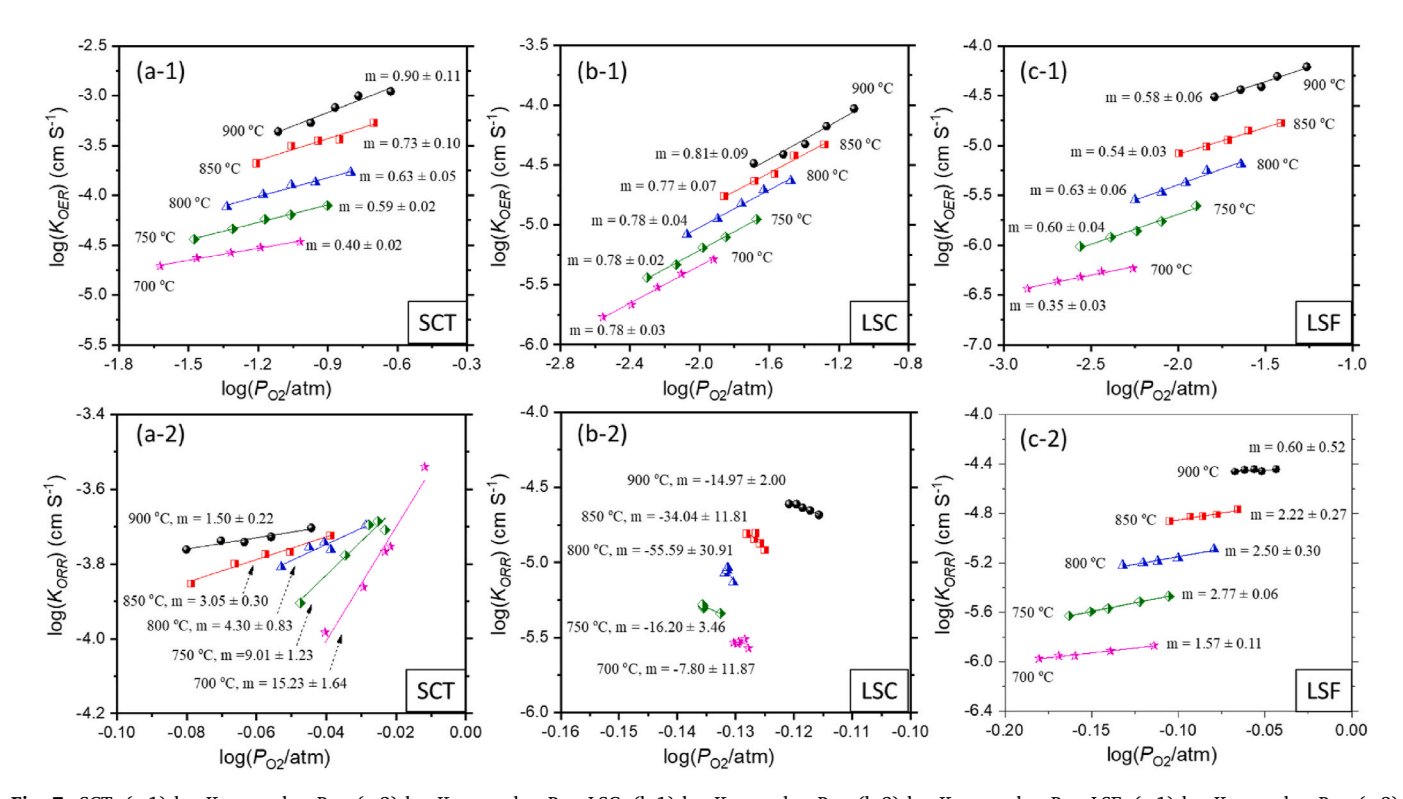


Fig. 7. SCT: (a-1)  $\log K_{OER}$  vs.  $\log P_{O_2}$ ; (a-2)  $\log K_{OER}$  vs.  $\log P_{O_2}$ . LSC: (b-1)  $\log K_{OER}$  vs.  $\log P_{O_2}$ ; (b-2)  $\log K_{ORR}$  vs.  $\log P_{O_2}$ . LSF: (c-1)  $\log K_{ORR}$  vs.  $\log P_{O_2}$ . LSF: (c-1)  $\log K_{ORR}$  vs.  $\log P_{O_2}$ . Note that the m values in (a-2), (b-2) and (c-2) might not be reliable due to the limitation of the method.

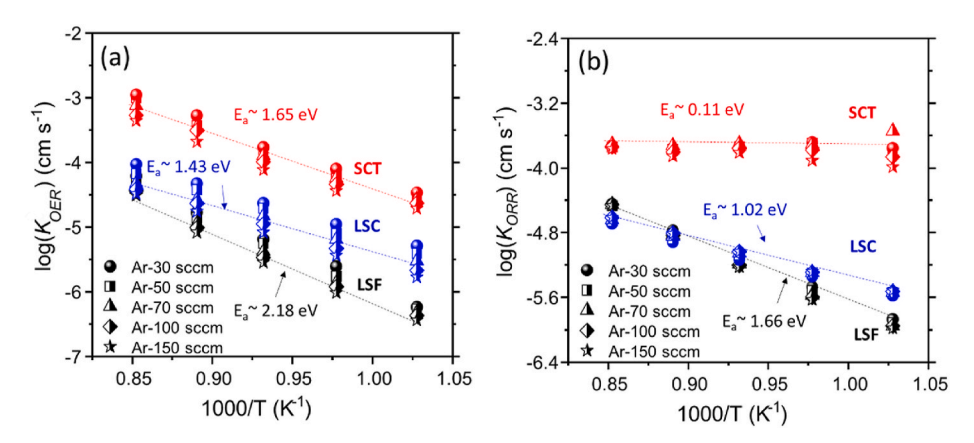


Fig. 8. Arrhenius plots of (a)  $K_{OER}$  and (b)  $K_{OER}$  for SCT, LSC and LSF.

nature of surface oxygen exchange kinetics. For  $K_{OER}$  data, all samples show positive power index m > 0 over a relatively broad  $P_{O_2}$  range, suggesting higher  $P_{O_2}$  favors the equilibrium rates of oxygen exchange

for OER. Most m-values fall between 0.5 and 1.0 (except for 700  $^{\circ}$ C), signaling that RLS is closely tied to the association of  $2O_{ad} = O_{2,ad}$  ( $O_{ad}$ : adsorbed O atom) and molecular desorption of  $O_{2,ad} = O_{2(g)}$  ( $O_{2,ad}$ :

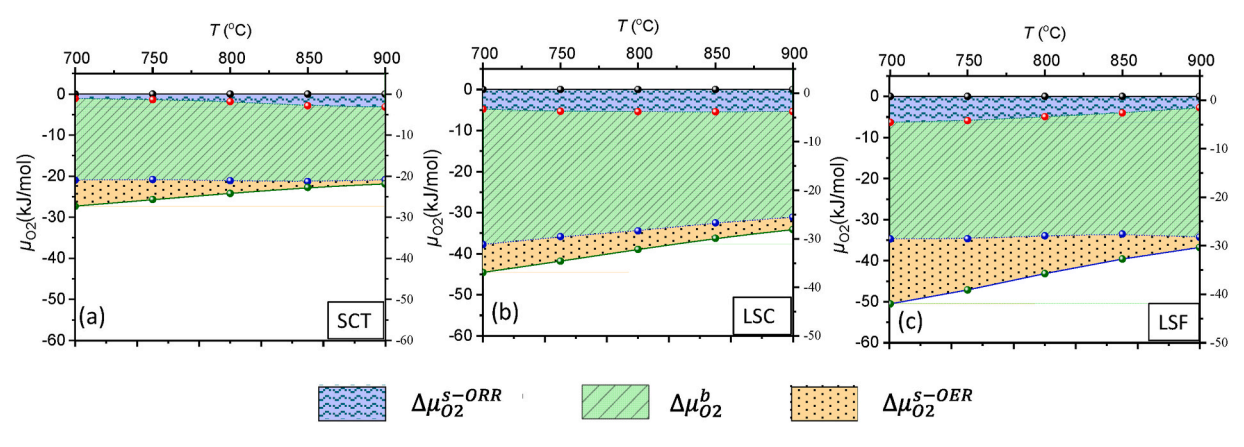


Fig. 9. Oxygen chemical potential gradient (in relative to air) of (a) SCT; (b) LSC and (c) LSF at  $P_{O_2-L}$  equivalent to Ar flow at 100 sccm.

adsorbed O<sub>2</sub>) [35,36]. Previous work [17] suggests that the range of m 0.39-0.41 for several electron-rich mixed conductors (e.g.,  $La_{0.8}Sr_{0.2}MnO_{3-\delta}$ ,  $La_{0.6}Sr_{0.4}Fe_{0.8}Co_{0.2}O_{3-\delta}$  and  $La_{0.3}Sr_{0.7}CoO_{3-\delta}$ ), lower than our results. This is mainly because K values were measured with isotope surface exchange method, which assumes the system is in equilibrium. In this work, K is measured under an active gradient of  $P_{O_2}$ , which is far from equilibrium. The m values here are close to Ref. [28] (~0.7 for La $_{0.6}Sr_{0.4}Fe_{0.6}Ga_{0.4}O_{3-\delta}$  and ~0.8 for La $_2NiO_{4+\delta}$ ), both of which used the oxygen permeation method. In contrast, the variations of  $K_{ORR}$  are limited within a much narrower  $P_{O_2}$  range for the three samples. The experiment has no control of this  $P_{O_2}$  range because  $P_{O_2}^{'}$  $(\Delta\mu_{O_2}^{s-ORR})$  at the ORR surface is passive and driven by the change of  $P_{O_2-L}$ . In other words, the resultant  $P'_{O_2}$  is controlled by the membrane's oxide-ion transport rate and the rate of oxygen exchange at the OER surface. A membrane with a high overall oxygen permeation flux  $(J_{O_2})$ would not require too much change in  $P_{O_2}^{'}$  ( $\Delta\mu_{O_2}^{s-ORR}$ ) at the feed-gas interface. The passive response of  $P_{O_2}^{'}$  within a very narrow  $P_{O_2}$  range (or very small  $\Delta \mu_{O_2}^{s-ORR}$  as shown in Fig. 9(a)) causes a significant level of uncertainty in determining  $K_{ORR}$  vs. log  $P_{O_2}$  relationship, which ultimately might lead to erroneously high absolute m values. Therefore, this could be a critical limitation to the present method to acquire the dependence of  $K_{ORR}$  vs.  $\log P_{O_2}$ . To obtain  $K_{ORR}$ -  $\log P_{O_2}$  relationship with high fidelity, a similar study but with systematically changing feed-side  $P_{O_2}$  might be needed.

The Arrhenius plots of  $K_{OER}$  and  $K_{ORR}$  of the three materials are shown in Fig. 8. The activation energy of  $K_{OER}$  is the lowest for LSC, followed by SCT and LSF, whereas that of  $K_{ORR}$  is the lowest for SCT, followed by LSC and LSF. Note that even though  $K_{ORR}$  vs.  $P_{O_2}$  relationship is questionable due to the small  $P_{O_2}$  range, its dependence on T still has the merit. For example, using the same OPC method, Yang et al. reported K=2.95 x  $10^{-3}$  cm/s (assuming  $K_{OER} = K_{ORR} = K$ ) for SCT [13]. With ECR method, Ganeshananthan et al. reported  $9.5 \times 10^{-5}$ ,  $1.5 \times 10^{-4}$  and  $3.1 \times 10^{-4}$  cm/s at 700, 750 and 800 °C, respectively, for LSC [37]. With ECR method, Søggaard et al. reported  $9.5 \times 10^{-5}$  and  $9.61 \times 10^{-5}$  cm/s at 800 and 900 °C, respectively, for LSF [32]. All these literature data are within the same order of magnitude to our data. The analytical expressions of  $K_{OER}$  and  $K_{ORR}$  as a function of  $P_{O_2}$  and temperature are listed in Table 1 for easy reference.

## 4.4. Oxygen chemical potential gradients across the membrane

With  $\mu_{O_2}^{g-ORR}$  at the feed-gas (air) side as the reference, the relative oxygen chemical potential across the three layers can be calculated out using eqs. (1), (2) and (12); the results are shown in Fig. 9 as a function of temperature for the case of Ar-100 as an example. The  $\Delta\mu$  profiles at other Ar flows (or sweep-side  $P_{O_2-L}$ ) are similar. For all three materials

studied,  $\Delta\mu_{O_2}^b$  are the highest compared to  $\Delta\mu_{O_2}^{s-ORR}$  and  $\Delta\mu_{O_2}^{s-OER}$ , which is understandable for the thick OTMs (1.5 mm) used in this study. Another observation is that  $\Delta\mu_{O_2}^{s-OER}$  is higher than  $\Delta\mu_{O_2}^{s-ORR}$  in all cases, implying that OER could be the predominant RLS in the overall surface oxygen exchange process. However, as the temperature increases, the difference between  $\Delta\mu_{O_2}^{s-OER}$  and  $\Delta\mu_{O_2}^{s-ORR}$  becomes smaller, inferring all surface reactions are thermally activated.

#### 4.5. B-transport numbers

With eqs. 13-15, the B-transport numbers have been calculated out; the results are shown in Fig. 10. From the total B-transport number,  $B_C$ , shown in Fig. 10(a-1), (b-1) and (c-1), it is evident that oxygen transport through SCT and LSC is not limited by the surface but the membrane bulk since their  $B_C$  values are lower than 0.5, whereas oxygen transport through LSF is limited by bulk diffusion together with the surface oxygen exchange. Looking into B-transport number in each individual surface layer, Fig. 10(a-2), (b-2), (c-2), (a-3), (b-3) and (c-3), it is evident that OER process is the real RLS in the surface oxygen exchange process since  $B_{C-ORR}$  is smaller than  $B_{C-OER}$ . For all the three materials tested, all  $B_{C-ORR}$  values are close; but the difference is in  $B_{C-OER}$ , particularly for LSF, which is understandable given the fact that LSF has the lowest oxide-ion conductivity. Overall, it is concluded that RLS for 1.5-mm thick SCT and LSC membranes is the bulk diffusion, whereas it is OER together with bulk diffusion for LSF, especially at lower temperatures. The determining factor of the difference is the level of partial oxide-ion conductivity in these membranes.

# 5. Conclusions

In summary, we have successfully obtained oxygen surface exchange and bulk transport properties of three well-known mixed oxide-ion and electron conducting membranes, namely, SCT, LSC and LSF, with a combined oxygen permeation cell and oxygen probe methodology. With this method, oxygen chemical potential gradients across the two oxygen exchange surface layers and one oxygen bulk diffusion layer are simultaneously measured, with which the rates of oxygen surface exchange at the two opposing membrane surfaces and oxide-ion conductivity/oxygen chemical diffusivity of the membrane bulk are obtained. The results show that SCT has the highest oxide-ion conductivity of 0.3  $\sim 1.2$  S/cm and oxygen chemical diffusivity of  $10^{\text{-}5} \sim 10^{\text{-}6} \text{ cm}^2\text{/s}$  with the lowest energy barrier of 0.71 eV over 700 – 900  $^{\circ}$ C, followed by LSC and LSF. This observation is well expected because SCT possesses the highest concentration of oxygen vacancies due to the strong Co-O-Co covalent interactions. Similarly, SCT also exhibits the highest rates of oxygen surface exchange of ORR and OER, reaching  $K_{OER} = 10^{-4} \sim 10^{-5}$ cm/s and  $K_{ORR} = 10^{-3} \sim 10^{-4}$  cm/s over 700 – 900 °C. Compared to ORR

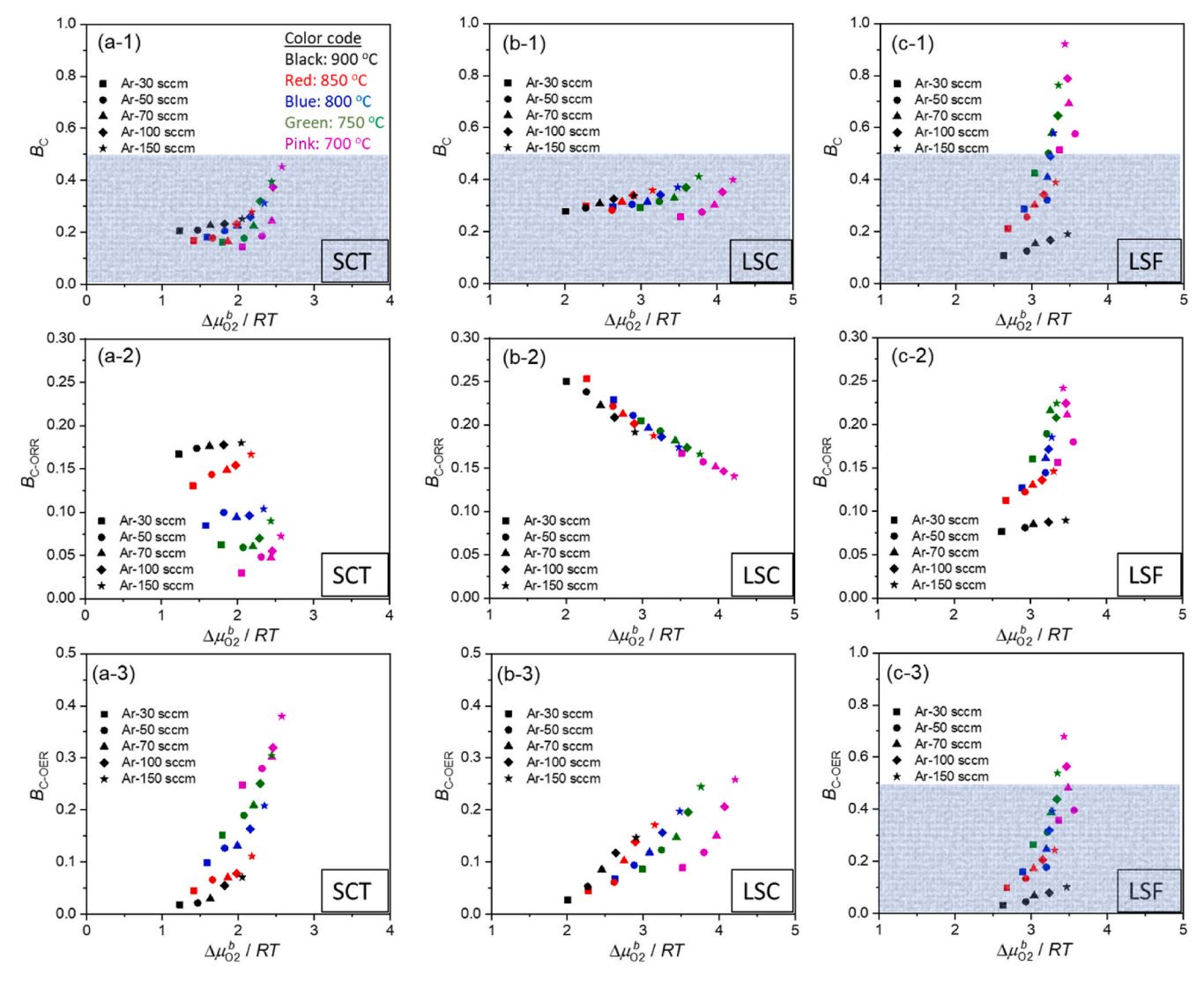


Fig. 10. B-transport numbers vs.  $\Delta \mu_{O_2}^b/RT$ . SCT: (a-1)  $B_C$ ; (a-2):  $B_{C-ORR}$ ; (a-3):  $B_{C-OER}$ . LSC: (b-1)  $B_C$ ; (b-2):  $B_{C-ORR}$ ; (b-3):  $B_{C-OER}$ . LSF: (c-1)  $B_C$ ; (c-2):  $B_{C-ORR}$ ; (c-3):  $B_{C-OER}$ .

kinetic rate, OER surface appears to be the most rate-limiting factor in the oxygen surface exchange process within the  $P_{O_2}$  range studied. The differences in bulk and surface transport properties of the three materials studied are fundamentally rooted in the level of partial oxide-ion conductivity and oxygen chemical potential gradients across the surface and bulk layers. The relative contributions from these layers can be conveniently represented by the B-transport numbers. Overall, this study has successfully demonstrated that the use of combined oxygen permeation cell and oxygen probe method can unlock important surface and bulk transport properties of mixed oxide-ion and electron conductors operated under real working conditions of oxygen electrocatalysis.

# Author's statement

Yongliang: performed experiments, data analysis and manuscript drafting.

**Kevin Huang:** supervising, conceptualization and finalizing manuscript.

### Declaration of competing interest

The authors declare that they have no known competing financial interests or personal relationships that could have appeared to influence

the work reported in this paper.

# Acknowledgements

This material is based upon work supported by the U.S. Department of Energy's Office of Energy Efficiency and Renewable Energy (EERE) under the Fuel Cell Technologies Office (FCTO) under Award Number DE-EE-0008842. We would also like to thank National Science Foundation for the financial support under award number 1801284.

#### Appendix A. Supplementary data

Supplementary data to this article can be found online at https://doi.org/10.1016/j.memsci.2021.120082.

#### References

- S.D. Ebbesen, S.H. Jensen, A. Hauch, M.B. Mogensen, High temperature electrolysis in alkaline cells, solid proton conducting cells, and solid oxide cells, Chem. Rev. 114 (2014) 10697–10734.
- [2] C. Wang, Y. Yu, J. Niu, Y. Liu, D. Bridges, X. Liu, J. Pooran, Y. Zhang, A. Hu, Recent progress of metal–air batteries—a mini review, Appl. Sci. 9 (2019) 2787.
- [3] Q. Jiang, S. Faraji, D.A. Slade, S.M. Stagg-Williams, A review of mixed ionic and electronic conducting ceramic membranes as oxygen sources for high-temperature reactors, Membr. Sci. Technol. 14 (2011) 235–273.

- [4] L. Heyne, Electrochemistry of mixed ionic-electronic conductors, in: Solid Electrolytes, Springer, 1977, pp. 169–221.
- [5] A. Jun, J. Kim, J. Shin, G. Kim, Perovskite as a cathode material: a review of its role in solid-oxide fuel cell technology, ChemElectroChem 3 (2016) 511–530.
- [6] J. Simböck, M. Ghiasi, S. Schönebaum, U. Simon, F.M. de Groot, R. Palkovits, Electronic parameters in cobalt-based perovskite-type oxides as descriptors for chemocatalytic reactions, Nat. Commun. 11 (2020) 1–10.
- [7] O. Haas, R. Struis, J. McBreen, Synchrotron X-ray absorption of LaCoO<sub>3</sub> perovskite, J. Solid State Chem. 177 (2004) 1000–1010.
- [8] Y. Orikasa, T. Ina, T. Nakao, A. Mineshige, K. Amezawa, M. Oishi, H. Arai, Z. Ogumi, Y. Uchimoto, X-ray absorption spectroscopic study on La0. 6Sr0. 4CoO<sub>3-δ</sub> cathode materials related with oxygen vacancy formation, J. Phys. Chem. C 115 (2011) 16433–16438.
- [9] J. Mizusaki, J. Tabuchi, T. Matsuura, S. Yamauchi, K. Fueki, Electrical conductivity and seebeck coefficient of nonstoichiometric La<sub>1-x</sub>Sr<sub>x</sub>CoO<sub>3-δ</sub>, J. Electrochem. Soc. 136 (1989) 2082.
- [10] J. Mizusaki, Y. Mima, S. Yamauchi, K. Fueki, H. Tagawa, Nonstoichiometry of the perovskite-type oxides La<sub>1-x</sub>Sr<sub>x</sub>CoO<sub>3-6</sub>, J. Solid State Chem. 80 (1989) 102–111.
- [11] M. Patrakeev, J. Bahteeva, E. Mitberg, I. Leonidov, V. Kozhevnikov, K. Poeppelmeier, Electron/hole and ion transport in La<sub>1-x</sub>Sr<sub>x</sub>FeO<sub>3-8</sub>, J. Solid State Chem. 172 (2003) 219–231.
- [12] T. Yang, Y. Wen, T. Wu, N. Xu, K. Huang, A highly active and Cr-resistant infiltrated cathode for practical solid oxide fuel cells, J. Mater. Chem. 8 (2020) 82–86.
- [13] T. Yang, X. Jin, K. Huang, Transport properties of SrCo<sub>0.9</sub>Nb<sub>0.1</sub>O<sub>3-δ</sub> and SrCo<sub>0.9</sub>Ta<sub>0.1</sub>O<sub>3-δ</sub> mixed conductors determined by combined oxygen permeation measurement and phenomenological modeling, J. Membr. Sci. 568 (2018) 47–54.
- [14] J. Wang, T. Yang, L. Lei, K. Huang, Ta-Doped SrCoO<sub>3-8</sub> as a promising bifunctional oxygen electrode for reversible solid oxide fuel cells: a focused study on stability, J. Mater. Chem. 5 (2017) 8989–9002.
- [15] R. Ganeshananthan, A.V. Virkar, Measurement of surface exchange coefficient on porous La<sub>0.6</sub>Sr<sub>0.4</sub>CoO<sub>3-δ</sub> samples by conductivity relaxation, J. Electrochem. Soc. 152 (2005) A1620.
- [16] S. Wang, A. Verma, Y. Yang, A. Jacobson, B. Abeles, The effect of the magnitude of the oxygen partial pressure change in electrical conductivity relaxation measurements: oxygen transport kinetics in La<sub>0.5</sub>Sr<sub>0.5</sub>CoO<sub>3-6</sub>, Solid State Ionics 140 (2001) 125–133.
- [17] R. De Souza, A universal empirical expression for the isotope surface exchange coefficients (k\*) of acceptor-doped perovskite and fluorite oxides, Phys. Chem. Chem. Phys. 8 (2006) 890–897.
- [18] J. Maier, Evaluation of transport parameters in the presence of defects with variable charges, Solid State Ionics 57 (1992) 71–76.
- [19] P.-M. Geffroy, A. Vivet, J. Fouletier, N. Richet, P. Del Gallo, T. Chartier, Influence of oxygen surface exchanges on Oxygen semi-permeation through La<sub>(1-x)</sub>Sr<sub>x</sub>Fe<sub>(1-y)</sub>Ga<sub>y</sub>O<sub>3-δ</sub> dense membrane, J. Electrochem. Soc. 158 (2011) B971.
- [20] P.-M. Geffroy, M. Reichmann, T. Chartier, J.-M. Bassat, J.-C. Grenier, Evaluating oxygen diffusion, surface exchange and oxygen semi-permeation in Ln<sub>2</sub>NiO<sub>4+δ</sub> membranes (Ln= La, Pr and Nd), J. Membr. Sci. 451 (2014) 234–242.

- [21] P.-M. Geffroy, A. Vivet, J. Fouletier, C. Steil, E. Blond, N. Richet, P. Del Gallo, T. Chartier, The impact of experimental factors on oxygen semi-permeation measurements, J. Electrochem. Soc. 160 (2012) F60.
- [22] P.J. Gellings, Handbook of Solid State Electrochemistry, CRC press, 2019.
- [23] A.J. Bard, L.R. Faulkner, Fundamentals and applications, Electrochem. Methods 2 (2001) 580–632.
- [24] X. Jin, J. Wang, K. Huang, Defect chemistry and transport properties of  $SrCo_{1-x}Ta_xO_{2.5+\delta}$  as a promising oxygen electrocatalyst for reversible solid oxide fuel cells, Solid State Ionics 309 (2017) 48–57.
- [25] M. Kuhn, S. Hashimoto, K. Sato, K. Yashiro, J. Mizusaki, Oxygen nonstoichiometry, thermo-chemical stability and lattice expansion of La<sub>0.6</sub>Sr<sub>0.4</sub>FeO<sub>3-δ</sub>, Solid State Ionics 195 (2011) 7–15.
- [26] M. Kuhn, S. Hashimoto, K. Sato, K. Yashiro, J. Mizusaki, Oxygen nonstoichiometry and thermo-chemical stability of La<sub>0.6</sub>Sr<sub>0.4</sub>CoO<sub>3-8</sub>, J. Solid State Chem. 197 (2013) 39, 45
- [27] A. Berenov, A. Atkinson, J. Kilner, E. Bucher, W. Sitte, Oxygen tracer diffusion and surface exchange kinetics in La<sub>0.6</sub>Sr<sub>0.4</sub>CoO<sub>3-\(\delta\)</sub>, Solid State Ionics 181 (2010) 210 226
- [28] P.M. Geffroy, L. Guironnet, H.J.M. Bouwmeester, T. Chartier, J.C. Grenier, J. M. Bassat, Influence of oxygen partial pressure on the oxygen diffusion and surface exchange coefficients in mixed conductors, J. Eur. Ceram. Soc. 39 (2019) 59–65.
- [29] I. Kagomiya, K. Takahashi, K.-i. Kakimoto, Oxide ion conduction and surface exchange reactions of mixed conductive La<sub>0.65</sub>Ca<sub>0.35</sub>FeO<sub>3−δ</sub> based on oxygen permeation study, Chem. Mater. 31 (2019) 10135–10142.
- [30] T. Yang, J. Wang, Y. Chen, K. An, D. Ma, T. Vogt, K. Huang, A combined variable-temperature neutron diffraction and thermogravimetric analysis study on a promising oxygen electrode, SrCo0. 9Nb0. 103– δ, for reversible solid oxide fuel cells, ACS Appl. Mater. Interfaces 9 (2017) 34855–34864.
- [31] K. Huang, J.B. Goodenough, Oxygen permeation through cobalt-containing perovskites: surface oxygen exchange vs. lattice oxygen diffusion, J. Electrochem. Soc. 148 (2001) E203.
- [32] M. Søgaard, P.V. Hendriksen, M. Mogensen, Oxygen nonstoichiometry and transport properties of strontium substituted lanthanum ferrite, J. Solid State Chem. 180 (2007) 1489–1503.
- [33] M. Søgaard, P.V. Hendriksen, M. Mogensen, F.W. Poulsen, E. Skou, Oxygen nonstoichiometry and transport properties of strontium substituted lanthanum cobaltite, Solid State Ionics 177 (2006) 3285–3296.
- [34] E. Deronzier, T. Chartier, P.-M. Geffroy, Oxygen semi-permeation properties of La1- xSrxFeO3- δ perovskite membranes under high oxygen gradient, J. Mater. Res. 35 (2020) 2506–2515.
- [35] M. Escudero, A. Aguadero, J.A. Alonso, L. Daza, A kinetic study of oxygen reduction reaction on La2NiO4 cathodes by means of impedance spectroscopy, J. Electroanal. Chem. 611 (2007) 107–116.
- [36] Y. Takeda, R. Kanno, M. Noda, Y. Tomida, O. Yamamoto, Cathodic polarization phenomena of perovskite oxide electrodes with stabilized zirconia, J. Electrochem. Soc. 134 (1987) 2656.
- [37] R. Ganeshananthan, A.V. Virkar, Measurement of transport properties by conductivity relaxation on dense La0. 6Sr0. 4CoO3–  $\delta$  with and without porous surface layers, J. Electrochem. Soc. 153 (2006) A2181.